

# Characterization of Nonlinear Angular Noise Coupling into Differential Arm Length of the LIGO Livingston Detector

Brian C. Seymour,<sup>1</sup> Marie Kasprzack,<sup>2</sup> Arnaud Pelé,<sup>2</sup> and Adam Mullavey<sup>2</sup>

<sup>1</sup>*LIGO SURF Student, University of Virginia\**

<sup>2</sup>*LIGO SURF Mentor, LIGO Livingston Observatory*

(Dated: September 23, 2017)

Mirror misalignments of the Fabry Perot Cavity mirrors can change the cavity length. This source of noise can couple into differential arm length of a gravitational wave detector. This paper explores length change due to nonlinear angular misalignment, and then extends it to the effect of angular noise on the two cavity system. We will also provide results from an experiment where we use mechanical modulation to measure the main angular components that are believed to couple most strongly to the differential arm length. The angular noise coupling model and experimental results will be used in combination to understand the nonlinear angular noise contribution to differential arm length noise.

---

\* [Seymour.BrianC@gmail.com](mailto:Seymour.BrianC@gmail.com)

## I. Introduction

In 1916 gravitational waves were predicted by Albert Einstein as a byproduct of his general theory of relativity which describes the relation between spacetime and matter. Just as accelerating charges emit light in classical electrodynamics, gravitational waves are emitted by accelerating masses. Gravitational waves travel at the speed of light in vacuum but, contrary to the latter, they are not obstructed by matter [1].

Gravitational waves will lead to new physics and astrophysics to examine the universe in complement to the existing information such as electromagnetic radiation and particles. Since gravity is much weaker than the other four fundamental forces, it is challenging to set up an experiment with gravity due to the large scale required to observe it. Thus, research in gravity is done by observing astrophysical signals around us, and gravitational waves will provide a new way to see more direct influences of the effects of gravity [2]. Additionally, predictions of general relativity can be compared to the gravitational wave data to test the validity limits of the theory. Lastly, gravitational wave astronomy will open a myriad of astronomical data, from examining black holes to probing past the cosmic microwave background. The cosmic microwave background may include a gravitational wave background, which would be evidence for inflation.

Laser Interferometer Gravitational-Wave Observatory (LIGO) is a collaboration dedicated to finding gravitational waves. It consists of two main facilities in Livingston, Louisiana and Hanford, Washington. These facilities detect gravitational waves with an optical system based on the interferometer developed by Michelson and Morley. Each observatory consists of a Michelson interferometer with 4 kilometer arms which measure the deformation of space produced by gravitational wave by looking for intensity variations in the interference pattern. It contains Fabry-Perot cavities which allows the light to bounce along the arms about 280 times. It uses light recycling to increase the power of a 25W laser into a 100KW laser in the arms. The laser also travels through a vacuum and dampens out environmental vibrations both actively and passively. The main optics are suspended with four stages of pendulums to passively isolate them from ground motion, and is kept at its operating point by active control through a plethora of feedback and feedforward techniques.

After LIGO searched for gravitational waves in the 2000's with no clear detections. Afterwards, the detectors were upgraded via the Advanced LIGO project. With these improvements, in September 2015, LIGO detected the first gravitational wave, and they had a second detection in December 2015 [3, 4]. Both of these detections were due to binary black hole system rotating and then combining.

In order to keep the mirrors stable, LIGO uses an active alignment sensing and control system (ASC) to reduce the mirror's angular motion [5]. Currently, the low frequency sensitivity (10-15 Hz) of the LIGO Livingston instrument is limited by the angular control feedback loops. To reduce the noise in this frequency band, the angular noise to DARM coupling should be reduced below 1/10th of the design sensitivity at that frequency [5].

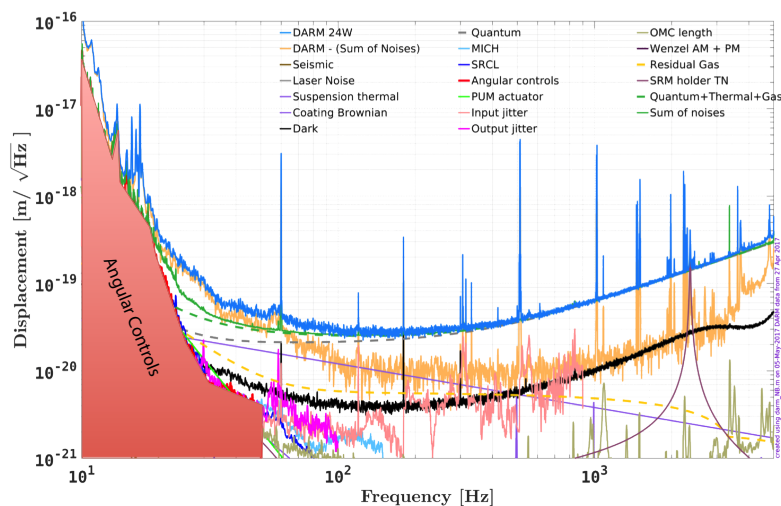


FIG. 1. Notice the sharp uptick in angular noise 25Hz, where it quickly becomes the dominant source of noise at 10Hz [6].

## II. Change in Cavity Length in Fabry-Perot Cavity

### II.1. Beam Spot Motion Approach to Angular Noise

In the interferometer cavity, angular rotations can create noise by coupling to cavity length. This is because the beam is not centered the mirror's center of rotation, and this distance is called static beam spot offset. When the mirror rotates slightly, this causes a change in cavity length (eq (1)). The equation depends on frequency however, and for the Fourier transform of equation (1), both the beam spot offset and mirror angle depend on frequency. The convolution can be approximated as in equation (2) [5].

$$\Delta l(t) = d_{spot}(t) \times \theta_{mirror}(t) \quad (1)$$

$$\begin{aligned} \Delta L(f) &= D_{spot}(f) * \Theta_{mirror}(f) \\ &\approx d_{spot}^{RMS} \times \Theta_{mirror}(f) + \theta_{mirror}^{RMS} \times D_{spot}(f) \end{aligned} \quad (2)$$

### II.2. Cavity Misalignments

A laser beam in the Fabry-Perot cavity is shifted away due to angular misalignment in the cavity mirrors. The length of the cavity that the light beam travels is changed. This manuscript will describe methods to deduce both the beam position displacement and corresponding length changes as shown in Figure 2. The resulting change in cavity length from both arms contributes to the noise seen by the DARM channel.

A beam in the Fabry-Perot cavity must go through the two centers of curvature of the mirrors. So, when the mirrors rotate, the coordinates of their centers of curvature change,  $C_1$  and  $C_2$ . This causes the beam path to change. These points describe a line for the beam. We desire to find the points  $P_1$  and  $P_2$  for a given rotation.

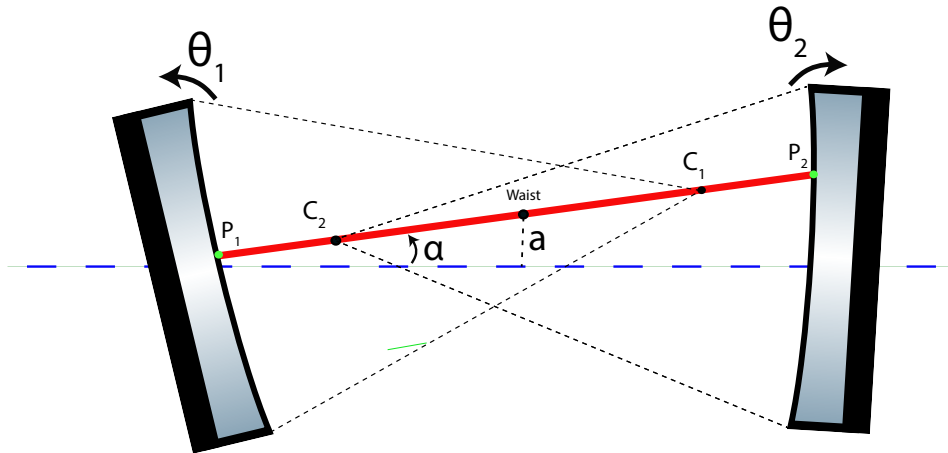


FIG. 2. This figure shows the setup of the mirrors. The points in the middle are the locations of the center of curvatures of each mirror. The points on the mirror are coordinates that this paper desires to find.

Where points in figure 2 are named as in equation (3).

$$\begin{aligned} C_1 &: (z_{1c}, x_{1c}) \\ C_2 &: (z_{2c}, x_{2c}) \\ P_1 &: (z_1, x_1) \\ P_2 &: (z_2, x_2) \end{aligned} \quad (3)$$

The waist rotation  $\alpha$  and the waist displacement  $a$  show how the waist changes in location with displacement. They will be discussed later.

### II.3. Change in Cavity Length

If a beam hits the mirrors at points  $P_1$  and  $P_2$ , the change in cavity length,  $\Delta L$ , can be found. Note, the angles and center of curvature coordinates are implicitly in the variables of equation (4). The initial cavity length before perturbation is  $L$ .

$$\Delta L = L' - L = \sqrt{(x_2 - x_1)^2 + (z_2 - z_1)^2} - L \quad (4)$$

### II.4. Beam Reflection Location in Fabry-Perot Cavity

The left mirror is the input test mass (ITM) in this paper and the right mirror is the end test mass (ETM). For notation simplicity, the ITM angle is  $\theta_1$  (CCW convention) and the ETM angle is  $\theta_2$  (CW convention) with both measuring the angular misalignment. Let  $x$  be the height of the beam at position  $z$  horizontally. The following constants are the locations of the center of curvature of mirror 1 and 2.

$$\begin{cases} z_{1c} = R_1 \cos(\theta_1) \\ x_{1c} = R_1 \sin(\theta_1) \\ z_{2c} = L - R_2 \cos(\theta_2) \\ x_{2c} = R_2 \sin(\theta_2) \end{cases} \quad (5)$$

The beam line pictured in red must go through the two centers of curvature. Therefore the slope,  $m$ , can be obtained.

$$\begin{aligned} m &= \frac{x_{1c} - x_{2c}}{z_{1c} - z_{2c}} \\ &= \frac{R_1 \sin(\theta_1) - R_2 \sin(\theta_2)}{R_1 \cos(\theta_1) + R_2 \cos(\theta_2) - L} \end{aligned} \quad (6)$$

The beam path is given in equation (7). The equations for the mirror curves are in equations (8) and (9).

$$\begin{cases} x_{beam}(z) = x_{1c} + m(z - z_{1c}) & (7) \\ R_1^2 = (x(z) - x_{1c})^2 + (z - z_{1c})^2 & (8) \\ R_2^2 = (x(z) - x_{2c})^2 + (z - z_{2c})^2 & (9) \end{cases}$$

What remains to be found is the points of intersection of the beam and the mirrors. Substituting  $x_{beam}(z)$  into the mirror equations, the solution emerges in equation (13):

$$R_1^2 = (x_{1c} + m(z - z_{1c}) - x_{1c})^2 + (z - z_{1c})^2 \quad (10)$$

$$R_1^2 = (m(z - z_{1c}))^2 + (z - z_{1c})^2 \quad (11)$$

$$R_1^2 = (m^2 + 1)(z - z_{1c})^2 \quad (12)$$

$$z = z_{1c} \pm \frac{R_1}{\sqrt{m^2 + 1}} \quad (13)$$

By symmetry the second intersection can be found. The extraneous roots are removed since the angle is less than  $\pi/2$  radians (eq (14a) and (14b)). The coordinates of the beam spot are  $(z_1, x(z_1))$  and  $(z_2, x(z_2))$ . Thus  $\Delta L$  can be determined from these coordinates when placed in (4).

$$z_1 = z_{1c} - \frac{R_1}{\sqrt{m^2 + 1}} \quad (14a)$$

$$z_2 = z_{2c} + \frac{R_2}{\sqrt{m^2 + 1}} \quad (14b)$$

## II.5. Change in Cavity Length to the Second Order

A second order approximation for equation (4) can be found around the point  $(\theta_1, \theta_2) = (0, 0)$  now that the values in equations (14a) and (14b) have been found. This is shown in equation (15). A discussion about how this was found is through Mathematica is located in appendix A. The  $g$  factors are unitless constants; in real system their values are:  $g_1 = g_{itm} = -1.0655$  and  $g_2 = g_{etm} = -.7794$  [7].

$$\begin{aligned} \Delta L \approx \Delta L_{2nd} &= \frac{L}{2(1 - g_1 g_2)} (g_2 \theta_1^2 + 2\theta_1 \theta_2 + g_1 \theta_2^2) \\ g_i &= 1 - \frac{L}{R_i} \end{aligned} \quad (15)$$

## III. Hard and Soft Basis

### III.1. Motivation of Hard-Soft Basis from Radiation Pressure

When the beam is not aligned with the cavity axis, the radiation pressure of the beam exerts a torque on the mirrors. This reduces the pendulum restoring torque by the mirror suspension which can increase misalignment. Radiation pressure torque depends on the beam spot displacement. Equation (17) shows the value of the radiation pressure torque as a function of angle by linking it with equation (16) [8].

$$\vec{x}_{sa} = \begin{bmatrix} x_{1,sa} \\ x_{2,sa} \end{bmatrix} = \frac{L}{1 - g_1 g_2} \begin{bmatrix} g_2 & 1 \\ 1 & g_1 \end{bmatrix} \begin{bmatrix} \theta_1 \\ \theta_2 \end{bmatrix} \quad (16)$$

$$\vec{\tau}_{opt} = \frac{2P}{c} \begin{bmatrix} x_1 \\ x_2 \end{bmatrix} = -\mathbf{K}_{opt} \begin{bmatrix} \theta_1 \\ \theta_2 \end{bmatrix} \quad (17)$$

Equation (17) gives a differential equation for torque. The hard-soft basis is one that diagonalizes the  $\mathbf{K}_{opt}$  matrix in order to solve the differential equation (18) [8]. Equation (19) is the change of basis matrix for the diagonalization [5].

$$\vec{\tau}_{ext} = \mathbf{I} \ddot{\vec{\theta}} + \gamma \dot{\vec{\theta}} + (\kappa_p + \mathbf{K}_{opt}) \vec{\theta} \quad (18)$$

$$\mathbf{S} = \begin{bmatrix} 1 & -r \\ r & 1 \end{bmatrix} \quad (19)$$

$$r = \frac{(g_1 - g_2) + \sqrt{(g_1 - g_2)^2 + 4}}{2} \quad (20)$$

As laser power increases in the cavity, eigenvectors of the  $\mathbf{K}_{opt}$  have a negative restoring spring constant. As radiation pressure increases, the eigenvalue for the spring constant  $k_{soft}$  decreases in equation (21). Thus, control systems designed to mitigate this are used to keep the mirror alignment at its operating point.

$$\mathbf{S} \times \mathbf{K}_{opt} \times \mathbf{S}^{-1} = \begin{bmatrix} k_{soft} & 0 \\ 0 & k_{hard} \end{bmatrix} \quad (21)$$

This radiation pressure example has motivated an interesting soft-hard basis with nice properties. The hard mode represents rotation of the cavity axis, and the soft mode represents a vertical displacement of the cavity axis. Figure 3 shows this.

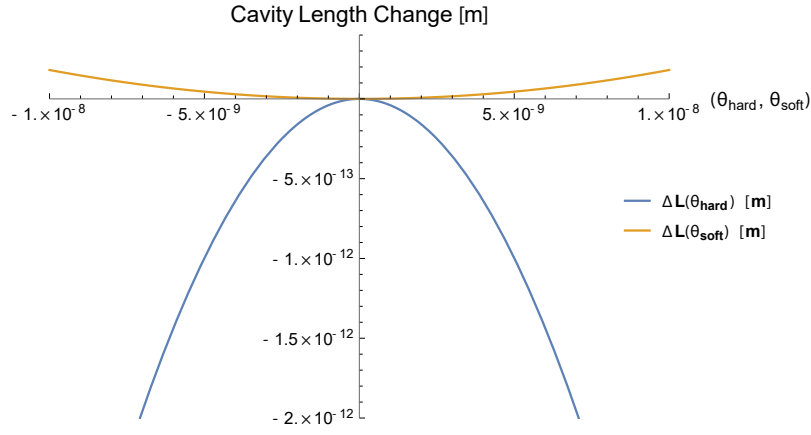


FIG. 4. This figure shows how the cavity length changes as a function of the soft and hard modes.

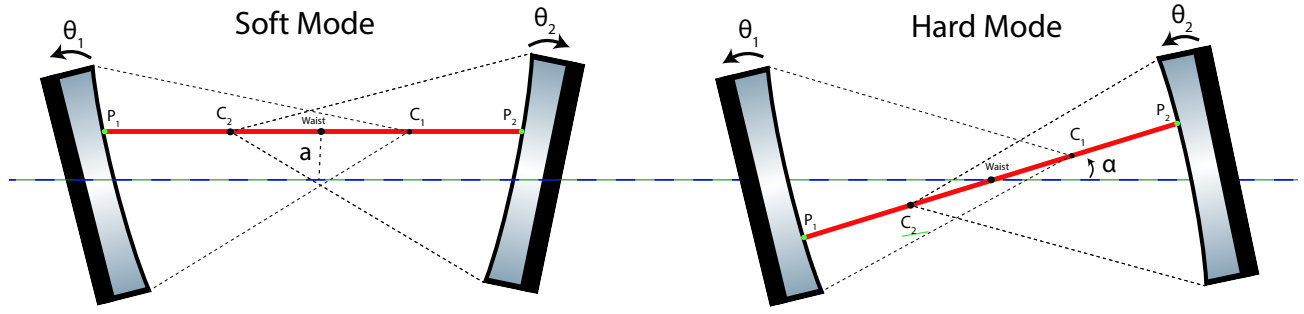


FIG. 3. This picture shows what the soft-hard basis angles look like in the cavity. This figure originated from page 7 in [5].

### III.2. The Cavity Length Change Approximation in Hard-Soft Basis

Cavity length change equation (15) can be converted into the hard-soft basis. Just as it diagonalized the radiation pressure matrix, it removes the cross terms from the cavity length change equation. The result is below in equation (22). The second equation includes the numerical values for the LIGO Livingston interferometer, which is calculated by using  $g$  factors and the initial cavity length.

$$\Delta L = \frac{L}{2(1 - g_1 g_2)} \left[ \theta_{soft}^2 (g_1 r^2 + 2r + g_2) + \theta_{hard}^2 (g_2 r^2 - 2r + g_1) \right] \quad (22)$$

$$\Delta L = 1810.49 \theta_{soft}^2 - 39883.9 \theta_{hard}^2 \quad (23)$$

This equation for hard and soft modes is shown in figure 4.

## IV. Two Cavity Picture for Angle-to-Length Coupling

### IV.1. Two Cavity DARM Coupling

Since the principle concern for angle to length coupling is it's effect on DARM, equation (15) can be extended to find the effect of its coupling to DARM by subtracting the X arm length change from the Y arm length change. The

resulting change in DARM due to angular noise is in equation (24).

$$\begin{aligned}\Delta D &= \Delta L_x - \Delta L_y \\ &= \frac{L}{2 - 2g_1g_2} \left( (\theta_{ex}^2 g_1 + 2\theta_{ex}\theta_{ix} + g_2\theta_{ix}^2) \right. \\ &\quad \left. - (\theta_{ey}^2 g_1 + 2\theta_{ey}\theta_{iy} + g_2\theta_{iy}^2) \right)\end{aligned}\quad (24)$$

#### IV.2. Pitch and Yaw Convention

Until this point, the paper has worked the pitch case. The coordinate systems of the test masses are local, with the normal vector  $\hat{z}$  pointing towards the other test mass and  $\hat{x}$  pointing up. Since  $\hat{y} = \hat{z} \times \hat{x}$ , the transverse unit vectors point in the opposite direction,  $\hat{y}_2 = -\hat{y}_1$ . Thus, the yaw change of basis matrix acquires an extra minus sign in the second column of equation (25b) [9]. The relationship between bases is in equation (25c).

$$\mathbf{S}_{pitch} = \begin{bmatrix} 1 & -r \\ r & 1 \end{bmatrix} \quad (25a)$$

$$\mathbf{S}_{yaw} = \begin{bmatrix} 1 & -r \\ -r & -1 \end{bmatrix} \quad (25b)$$

$$\vec{\theta} = \begin{bmatrix} \theta_1 \\ \theta_2 \end{bmatrix} = \mathbf{S} \times \begin{bmatrix} \theta_{soft} \\ \theta_{hard} \end{bmatrix} = \mathbf{S} \times \vec{\theta}' \quad (25c)$$

#### IV.3. Differential/Common Hard/Soft Basis

In the two cavity case, it is useful to separate the hard/soft basis in cavity X and Y into the differential/common modes. For example, differential hard is X hard minus Y hard. The change of basis matrix is in equation (26). [5]:

$$\begin{pmatrix} \theta_{dif,h} \\ \theta_{dif,s} \\ \theta_{com,h} \\ \theta_{com,s} \end{pmatrix} = \frac{1}{2} \begin{pmatrix} 0 & 0 & 1 & -1 \\ 1 & -1 & 0 & 0 \\ 0 & 0 & 1 & 1 \\ 1 & 1 & 0 & 0 \end{pmatrix} \begin{pmatrix} \theta_{s,x} \\ \theta_{s,y} \\ \theta_{h,x} \\ \theta_{h,y} \end{pmatrix} \quad (26)$$

Equation (27) shows how the differential hard basis is related back to the mirror basis for both pitch and yaw [5]

$$\begin{pmatrix} \theta_{ix} \\ \theta_{iy} \\ \theta_{ex} \\ \theta_{ey} \end{pmatrix}_p = \begin{pmatrix} -r & 1 & -r & 1 \\ r & -1 & -r & 1 \\ 1 & r & 1 & r \\ -1 & -r & 1 & r \end{pmatrix} \begin{pmatrix} \theta_{dh} \\ \theta_{ds} \\ \theta_{ch} \\ \theta_{cs} \end{pmatrix}_p \quad (27a)$$

$$\vec{\theta}'_p = \mathbf{Q}_p \cdot \vec{\theta}'_p$$

$$\begin{pmatrix} \theta_{ix} \\ \theta_{iy} \\ \theta_{ex} \\ \theta_{ey} \end{pmatrix}_y = \begin{pmatrix} r & 1 & r & 1 \\ r & 1 & -r & -1 \\ 1 & -r & 1 & -r \\ 1 & -r & -1 & r \end{pmatrix} \begin{pmatrix} \theta_{dh} \\ \theta_{ds} \\ \theta_{ch} \\ \theta_{cs} \end{pmatrix}_y \quad (27b)$$

$$\vec{\theta}'_y = \mathbf{Q}_y \cdot \vec{\theta}'_y$$

Equation (24) for angular noise DARM coupling becomes equation (28) in the differential hard basis angular coupling to DARM. In  $\beta$ , pitch is + and yaw is -. Interestingly, the all the terms are multiples of common times differential modes.

Appendix E discusses CARM with the opposite case, where terms are multiples of only common times common and differential times differential modes.

$$\Delta D = \alpha \theta_{ch} \theta_{dh} + \beta \theta_{ch} \theta_{ds} + \beta \theta_{cs} \theta_{dh} + \gamma \theta_{cs} \theta_{ds} \quad (28a)$$

$$\mu = \frac{2L}{-1 + g_1 g_2} \quad (28b)$$

$$\alpha = \mu(-g_1 r^2 - g_2 + 2r) = -156191 \quad (28c)$$

$$\beta = \pm \mu(-g_1 r + g_2 r - r^2 + 1) = \pm 23379.1 \quad (28d)$$

$$\gamma = \mu(-r(g_2 r + 2) - g_1) = 3897.58 \quad (28e)$$

#### IV.4. Spectra of Angle to DARM Coupling

Consider the following situation where the DARM coupling is expressed as follows:

$$\Delta D(t) = \alpha \theta_{dh}(t) \theta_{ch}(t) \quad (29)$$

In the frequency domain:

$$\Delta D(f) = \alpha \hat{\theta}_{dh}(f) \star \hat{\theta}_{ch}(f) \quad (30)$$

Unfortunately, we are in the same situation as equation (2) where the convolution presents a problem. Thus to understand the effect on DARM of angular misalignment, the spectra of angles in the hard-soft basis must be found.

### V. Finding Spectra through Mechanical Modulation

In order to measure the spectra of the angles of the hard-soft basis, mechanical modulation will be used. Currently, the ADS system is used to align the cavity by modulation/demodulation at frequencies of 7 Hz, below the detection band. The demodulated output effectively measures the perturbation of the degree of freedom. This sensing method is similar to the optical modulation methods in the WFS and allows the actuators to correct for errors [10]. Appendix C gives an example of how mechanical modulation is used in LIGO to detect misalignments.

We will use this sensing method by dithering at a higher frequency to measure the spectra of the differential hard, differential soft, common hard, and common soft angular degrees of freedom. The dithering frequency used in the experiment was 48.7 Hz. Our witness is DARM channel which is demodulated and applied with a lowpass filter.

#### V.1. Mirror Angle Modulation Coupling to DARM

Equation (28) links the mirror degrees of freedom to change in DARM. Each degree of freedom is dithered according to the dithering parameters in 31a.  $\Theta(t)$  is the residual motion of the mirror which causes misalignment and the  $\sin \Omega t$  term is the dithering term from our hardware injection. The DARM channel is multiplied by (31b) in order to demodulate it.

$$\begin{aligned} \theta_{dh}(t) &= \Theta_{dh}(t) + A_{dh} \sin \Omega t \\ \theta_{ds}(t) &= \Theta_{ds}(t) + A_{ds} \sin \Omega t \\ \theta_{ch}(t) &= \Theta_{ch}(t) + A_{ch} \sin \Omega t \\ \theta_{cs}(t) &= \Theta_{cs}(t) + A_{cs} \sin \Omega t \end{aligned} \quad (31a)$$

$$O_{dmod} = A_{dmod} \sin \Omega t \quad (31b)$$

After modulating and demodulating equation (28) a lowpass filter is applied. The lowpass filter should reject all contributions from an  $\Omega$  term and above. The result of this lowpass filter is equation (32). The each angle's coefficient



for this equation is shown below in [32b](#). Note how this resulting spectra is a linear combination of all the degrees of freedom. We would like to find, however, the spectra of each mode. Therefore, the correct combination of amplitudes must be derived to get purely differential hard motion/etc.

$$\begin{aligned} \text{LP}(\Delta D \cdot O_{\text{dmod}}) &= C_{dh}\Theta_{dh} + C_{ds}\Theta_{ds} \\ &+ C_{ch}\Theta_{ch} + C_{cs}\Theta_{cs} \end{aligned} \quad (32a)$$

$$\begin{cases} C_{dh} = \frac{A_{\text{dmod}}}{2} (\alpha A_{ch} + \beta A_{cs}) \\ C_{ds} = \frac{A_{\text{dmod}}}{2} (\beta A_{ch} + \gamma A_{cs}) \\ C_{ch} = \frac{A_{\text{dmod}}}{2} (\alpha A_{dh} + \beta A_{ds}) \\ C_{cs} = \frac{A_{\text{dmod}}}{2} (\beta A_{dh} + \gamma A_{ds}) \end{cases} \quad (32b)$$

## V.2. Finding Spectra of Individual Modes

Since the constants in [32b](#) are functions of the dithering amplitudes of each mode, the amplitudes can be chosen to zero out all but one of the coefficients. This desired modulation acquires the desired output which is only dependent on one mode. This section will discuss how to pick the correct amplitudes. First, a linear system is set up.

$$\begin{pmatrix} C_{dh} \\ C_{ds} \\ C_{ch} \\ C_{cs} \end{pmatrix} = \frac{A_{\text{dmod}}}{2} \begin{pmatrix} 0 & 0 & \alpha & \beta \\ 0 & 0 & \beta & \gamma \\ \alpha & \beta & 0 & 0 \\ \beta & \gamma & 0 & 0 \end{pmatrix} \cdot \begin{pmatrix} A_{dh} \\ A_{ds} \\ A_{ch} \\ A_{cs} \end{pmatrix} \quad (33)$$

Since we desire to find the amplitudes in terms of the coefficients, the system is inverted. This system shows how to choose dithering amplitudes for a desired demodulated result. For example, by setting  $C_{dh}$  to 1 and the other constants to zero, the resulting spectrum is proportional to  $\Theta_{dh}$  in the demodulated output. This amplitude selection is a convenient way to measure spectra. (from now on,  $A_{\text{dmod}}$  will be set equal to 1)

$$\begin{pmatrix} A_{dh} \\ A_{ds} \\ A_{ch} \\ A_{cs} \end{pmatrix} = \frac{2}{\alpha\gamma - \beta^2} \begin{pmatrix} 0 & 0 & \gamma & -\beta \\ 0 & 0 & -\beta & \alpha \\ \gamma & -\beta & 0 & 0 \\ -\beta & \alpha & 0 & 0 \end{pmatrix} \begin{pmatrix} C_{dh} \\ C_{ds} \\ C_{ch} \\ C_{cs} \end{pmatrix} \quad (34)$$

Since the mirrors are driven according to their own local angles, the change of basis matrix  $\mathbf{Q}$  from equation [\(28\)](#) is used. Equations [\(35\)](#) and [\(36\)](#) give these modulation amplitudes in the local mirror angle basis. The full form of these matrices is given in appendix [B](#).

$$\begin{pmatrix} A_{ix} \\ A_{iy} \\ A_{ex} \\ A_{ey} \end{pmatrix}_p = \frac{2}{\alpha\gamma - \beta^2} \mathbf{Q}_p \cdot \begin{pmatrix} 0 & 0 & \gamma & -\beta \\ 0 & 0 & -\beta & \alpha \\ \gamma & -\beta & 0 & 0 \\ -\beta & \alpha & 0 & 0 \end{pmatrix} \begin{pmatrix} C_{dh} \\ C_{ds} \\ C_{ch} \\ C_{cs} \end{pmatrix}_p \quad (35)$$

$$\begin{pmatrix} A_{ix} \\ A_{iy} \\ A_{ex} \\ A_{ey} \end{pmatrix}_y = \frac{2}{\alpha\gamma - \beta^2} \mathbf{Q}_y \cdot \begin{pmatrix} 0 & 0 & \gamma & -\beta \\ 0 & 0 & -\beta & \alpha \\ \gamma & -\beta & 0 & 0 \\ -\beta & \alpha & 0 & 0 \end{pmatrix} \begin{pmatrix} C_{dh} \\ C_{ds} \\ C_{ch} \\ C_{cs} \end{pmatrix}_y \quad (36)$$

For example, to get the correct amplitude parameters for purely differential hard motion is found by setting  $(C_{dh}, C_{ds}, C_{ch}, C_{cs}) = (1, 0, 0, 0)$  and doing the appropriate matrix computations. We repeat the dithering for differential hard, differential soft, common hard, and common soft to get the residual spectra for each. These are then put into the model to predict the nonlinear angular noise coupling into DARM.

### V.3. Mirror Angle Calibration

In order to change the angle of a test mass, the penultimate test mass (PUM) actuators apply a torque. The torque arm distance is  $\frac{d}{\sqrt{2}}$  and there are torques applied in the OSEM system, where  $d = 100\text{mm}$ . Equation (37) gives the amount of angle change due to the counts. It is from equation 44 of [9].  $\text{TF}(f)$  is the transfer function between torque on the penultimate test mass to angle of the end test mass. It was calculated by a model detailed in that paper [9]. At  $f = 48.7\text{Hz}$ , the result is:

$$\begin{aligned} C_\theta &= 2\sqrt{2} * d * F_0 * \text{TF}_\theta(f) \\ C_\theta &= 1.694 \times 10^{-18} \frac{\text{rad}}{\text{cts}} \end{aligned} \quad (37a)$$

$$\begin{aligned} C_\phi &= 2\sqrt{2} * d * F_0 * \text{TF}_\phi(f) \\ C_\phi &= 2.074 \times 10^{-18} \frac{\text{rad}}{\text{cts}} \end{aligned} \quad (37b)$$

$F_0$  is created by a digital signal which is converted into volts, which is converted into current, which is used to create a magnetic field. This magnetic field exerts a force on the PUM. The numerical values are shown in equation (38), which are found in [11].

$$\begin{aligned} F_0 &= \frac{20 \text{ V}}{2^{18} \text{ cts}} \cdot 0.268 \frac{\text{mA}}{\text{V}} \cdot 0.0309 \frac{\text{N}}{\text{A}} \\ &= 6.318 \times 10^{-10} \frac{\text{N}}{\text{cts}} \end{aligned} \quad (38)$$

Thus, equation (39) shows the formula for the calibrated  $C_{dh}$  in pitch, where  $(a_{ch}, a_{cs})$  are the uncalibrated modulation amplitudes.

$$C_{dh} = A_{dmod} \cdot \frac{C_\theta}{2} (\alpha a_{ch} + \beta a_{cs}) \quad (39)$$

Appendix D gives a calibration flowchart summarizing this calibration process.

### V.4. Amplitude Spectrum Measurement for a Mode

In order to get the spectra of the differential hard mode, the amplitudes are set accordingly. The resulting equation of the measurement is in equation (40).  $\mathcal{A}(f)$  is the measurement of the demodulated DARM channel's amplitude spectral density in counts, and  $C_{\mathcal{A}}$  is the calibration.

$$\Theta_{dh}(f) = \frac{C_{\mathcal{A}}}{C_{dh}} \cdot \mathcal{A}(f) \quad (40)$$

$$\frac{1}{C_{\mathcal{A}}} = 6 \times 10^{17} \frac{\text{cts}}{\text{m}}$$

The result of the dithering technique is shown in figure 5 which shows the spectrum of the calibrated signal. Above 3 Hz, the DARM demodulation sensor cannot detect our injected modulation above the DARM noise floor. We can not modulate at a higher amplitude because the sensor is nearly saturated at lower frequencies. These constraints prevent any configuration of the dither technique from measuring mirror movements above 3 Hz. Since we are interested in angular noise up to 15 Hz, the 3 Hz noise barrier presents a problem.

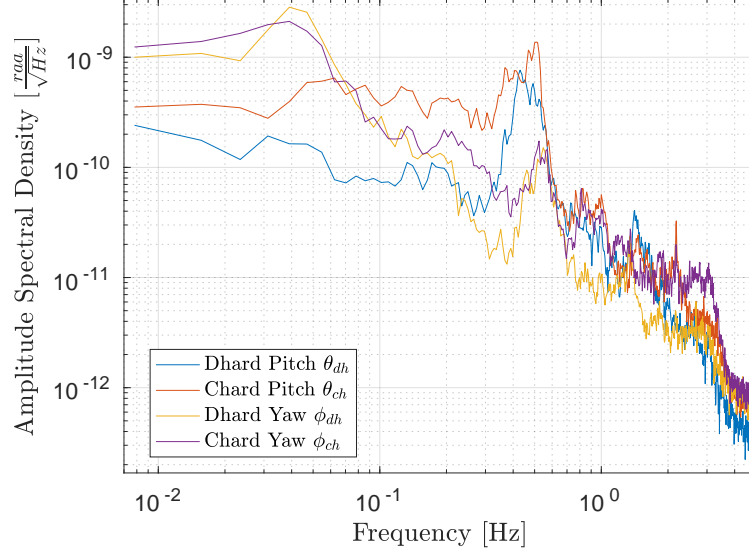


FIG. 5. This figure shows the result for the measured spectra. Above 3 Hz the signal is mostly noise.

## VI. Higher Frequency Angular Spectrum

Because the previous data is limited by noise below 3 Hz, we will use the Transmon QPDs (in figure 6) for measuring high frequency mode spectrum. By matching the low frequency spectrum obtained by mechanical modulation and the Transmon QPD sensors, we can get the mode spectrum to higher frequencies. This section will discuss two methods. The first that we used was Wiener filtering. Due to insufficiently long measurements, the Wiener filters overfit the data in this experiment and didn't work here. Secondly, we tried a simpler fit by measuring the linear combination of Transmon QPD signals which have the least error compared to the target signal. This method worked the best.

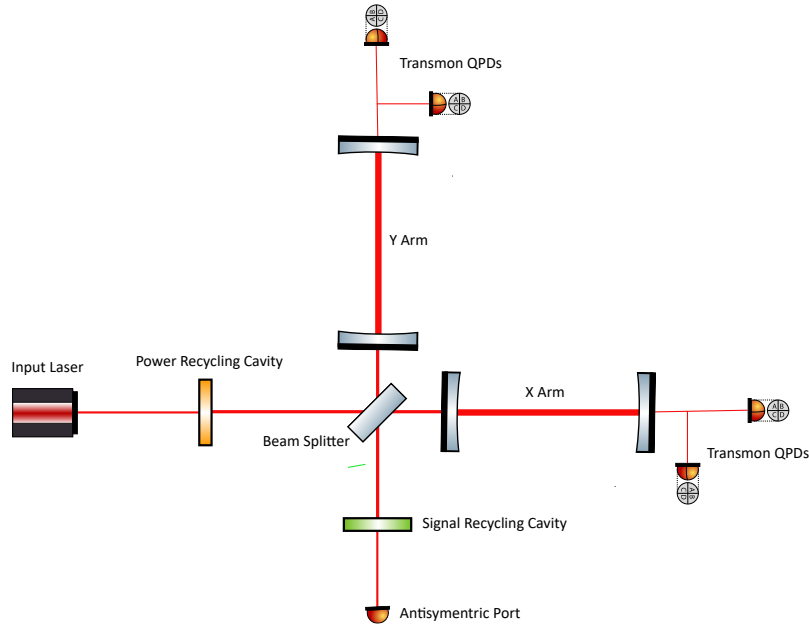


FIG. 6. This shows the location of the Transmon QPD witness sensors for the Wiener filter.

### VI.1. Wiener Filtering for Angular Noise

In this application, the witness signals are the the Transmon QPD signals, as shown in figure 6. There are four of them. We use a Matlab script to find the Wiener filters for each witness sensor. Figure 7 gives a visual demonstration of the Wiener filter. A more detailed discussion of the theory of Wiener Filtering is in appendix F.

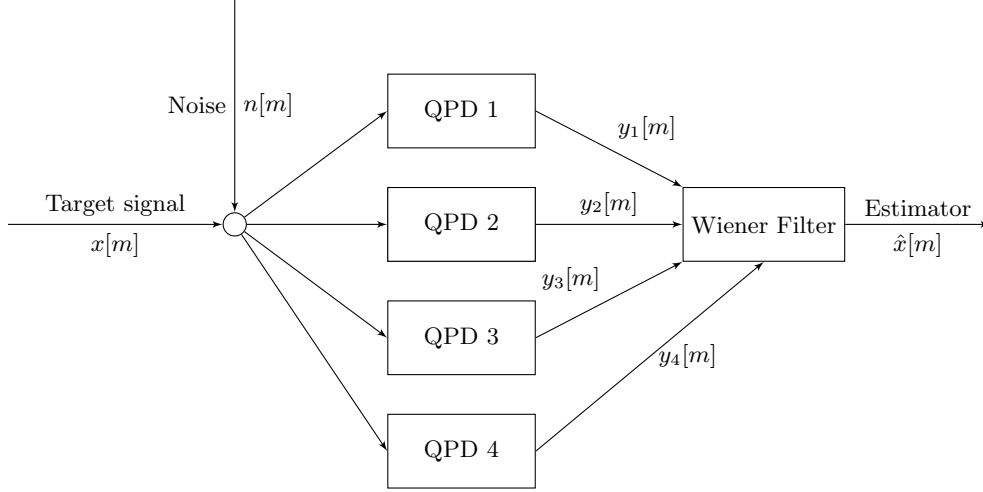


FIG. 7. This shows our setup for Wiener filtering the angular noise.

### VI.2. Wiener Filtering Results

The following results show the target (the dithering measurement) and estimator (from Wiener filter of QPDs) in a plot. They also show the coherence at each frequency. Even though this looks like a good estimation, it suffers from over fitting by closer examination of the filter.

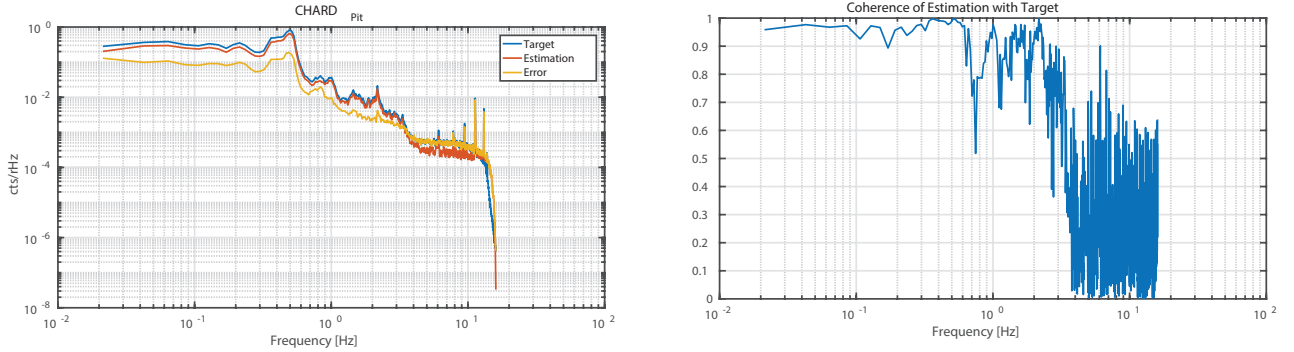


FIG. 8. Wiener Filter results

### VI.3. Least Mean Square Linear Combination Fit

To reduce the effect of over fitting the data, we replaced the Wiener filter estimation a simpler method of minimizing the linear combination of the QPD signals minus the target signal. The matching was done for frequencies below 1 Hz since the dithering sensing has the highest SNR here. Figure 9 shows the least mean square fit in red, which is used to generate the matched QPD signal in yellow. This signal has a higher noise cut off than the Wiener filter at about 9 Hz.

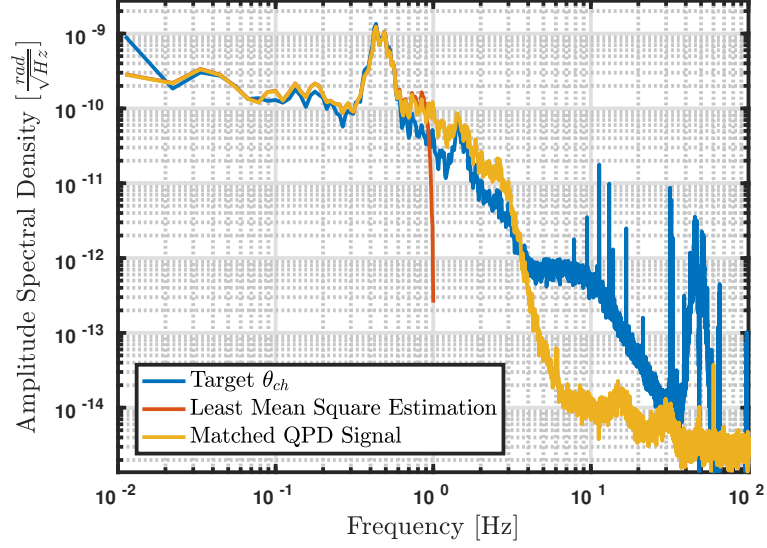


FIG. 9. The target is dithering measurement, the least mean square estimation is found by only considering 0-1Hz, and the matched QPD signal shows the resulting estimation.

## VII. Results

The angular modes found by the least mean square fit are shown in figure 10. Interestingly, the soft modes are higher than the hard modes.

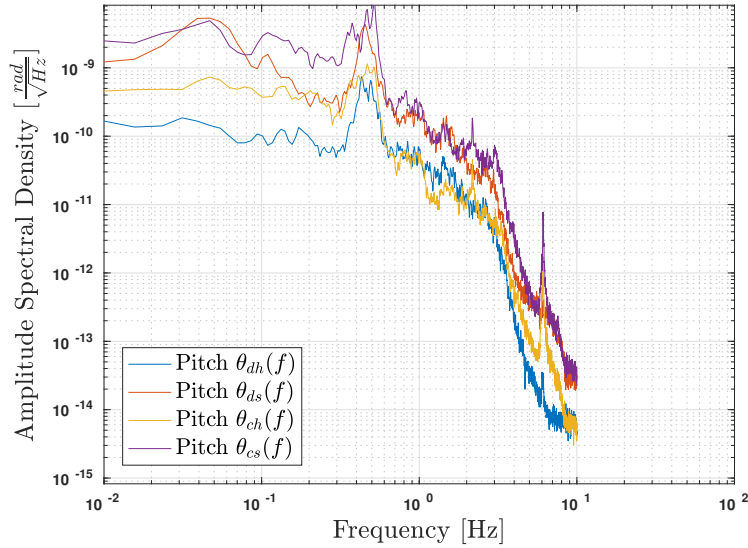


FIG. 10. Pitch spectra from combination of dithering and Transmon QPDs

Using the equation for DARM noise found earlier,

$$\Delta \text{DARM} = \alpha \theta_{ch} \theta_{dh} + \beta \theta_{ch} \theta_{ds} + \beta \theta_{cs} \theta_{dh} + \gamma \theta_{cs} \theta_{ds}$$

With the following approximation,

$$\mathcal{F}(\theta_1(t) \cdot \theta_2(t)) \approx \theta_2^{RMS} \theta_1(f) + \theta_1^{RMS} \theta_2(f)$$

The nonlinear noise contribution to DARM spectra can be found. Figure 11 shows the resulting coupling to DARM by the angular spectra found before.

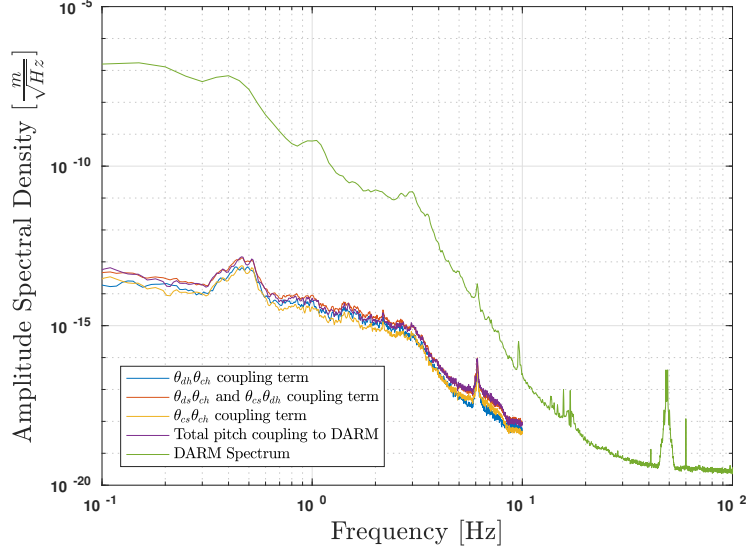


FIG. 11. Nonlinear angular noise, pitch

### VIII. Conclusion/Future Inquiry

In this paper, a model for angular misalignment DARM coupling was found. It also presents a technique to measure the nonlinear coupling of the angular noise by the dithering technique. We use this technique to find the angular spectra at low frequencies and matched these with Transmon QPDs to get it at higher frequencies. By the methods used here, we find that the nonlinear angular noise is a small contributor to DARM.

In the future, the angular spectra found by dithering and Transmon QPDs should be compared to other measurements and models. Additionally, the techniques used here to derive the angular coupling to DARM should be extended to the full interferometer's components.

## Acknowledgments

I would like to express my sincere gratitude to my mentors, Arnaud Pelé, Marie Kasprzack, and Adam Mullavey for providing me the opportunity for this summer research and for their time and energy. I am also thankful to spend my time at the LIGO Livingston through the Caltech LIGO SURF program. Without these institutions and people in them, I would not have been able to have such an amazing research experience in gravitational wave astronomy.

- 
- [1] R Kinney, A Weinstein, O Miyakawa, and R Ward. Development of Noise Budgets for the LIGO 40m IFO SURF 2005. *LIGO Document Control Center*, page T050149, 6 2005. URL: <https://dcc.ligo.org/LIGO-T050149>.
  - [2] Peter Saulson. *Fundamentals of Interferometric Gravitational Wave Detectors*. World Scientific, 1994. doi:10.1142/9789814350235.
  - [3] B. P. Abbott. Observation of gravitational waves from a binary black hole merger. *Physical Review Letters*, 116(6):61102, 2 2016. doi:10.1103/PhysRevLett.116.061102.
  - [4] B. P. Abbott and Et Al. GW151226: Observation of Gravitational Waves from a 22-Solar-Mass Binary Black Hole Coalescence. *Physical Review Letters*, 116(24):241103, 6 2016. doi:10.1103/PhysRevLett.116.241103.
  - [5] Lisa Barsotti and Matt Evans. Modeling of Alignment Sensing and Control for Advanced LIGO. *LIGO Document Control Center*, page T0900511\_v4, 2009. URL: <https://dcc.ligo.org/LIGO-T0900511>.
  - [6] Gabriele Vajente. The Advanced LIGO Noise Curve. *LIGO Document Control Center*, pages G1701262–v1, 2017. URL: <https://dcc.ligo.org/G1701262>.
  - [7] Katherine L Dooley, Lisa Barsotti, Rana X Adhikari, et al. Angular control of optical cavities in a radiation-pressure-dominated regime: the Enhanced LIGO case. *J. Opt. Soc. Am. A*, 30(12):2618–2626, 12 2013. URL: <http://josaa.osa.org/abstract.cfm?URI=josaa-30-12-2618>, doi:10.1364/JOSAA.30.002618.
  - [8] Katherine Dooley. *Design and Performance of High Laser Power Interferometers for Gravitational-wave Detection*. University of Florida, 2011.
  - [9] Marie Kasprzack and Hang Yu. Beam Position from Angle to Length Minimization. *LIGO Document Control Center*, page T1600397, 2016. URL: <https://dcc.ligo.org/T1600397>.
  - [10] K Kawabe, N Mio, and K Tsubono. Automatic alignment-control system for a suspended Fabry-Perot cavity. *Applied optics*, 33(24):5498–5505, 8 1994. URL: <http://ao.osa.org/abstract.cfm?URI=ao-33-24-5498>, doi:10.1364/AO.33.005498.
  - [11] Jeffery Kissel. aLIGO QUAD Controls Design Description. *LIGO Document Control Center*, page T1100378, 2016. URL: <https://dcc.ligo.org/LIGO-T1100378>.
  - [12] S V Vaseghi. *Advanced Digital Signal Processing and Noise Reduction*. 2009. URL: <http://www.scopus.com/inward/record.url?eid=2-s2.0-84889779628&partnerID=tZ0tx3y1>, doi:10.1002/9780470740156.
  - [13] Jennifer C. Driggers, Matthew Evans, Keenan Pepper, and Rana Adhikari. Active noise cancellation in a suspended interferometer. *Review of Scientific Instruments*, 83(2):1–7, 3 2012. doi:10.1063/1.3675891.
  - [14] Michael Coughlin, Jan Harms, Nelson Christensen, et al. Wiener filtering with a seismic underground array at the Sanford Underground Research Facility. *Classical and Quantum Gravity*, 215003(21):1–26, 2014. URL: <http://arxiv.org/abs/1403.7756v5><http://dx.doi.org/10.1088/0264-9381/31/21/215003>, doi:10.1088/0264-9381/31/21/215003.
  - [15] V Tiwari, M Drago, V Frolov, and others. Regression of environmental noise in LIGO data. *Classical and Quantum Gravity*, 32(16):165014, 2015. URL: <http://stacks.iop.org/0264-9381/32/i=16/a=165014>.

### A. Exact Results from Mathematica

This appendix has the exact values of the coordinates found in section II.4. It also has the full equation for  $\Delta L$  that was found. Equation (A1) was used in Mathematica to find the Taylor series in equation (15) from section II.5.

$$\Delta L = \text{Abs} \left( L \sqrt{\frac{(R_1 \sin(\theta_1) - R_2 \sin(\theta_2))^2}{(-L + R_1 \cos(\theta_1) + R_2 \cos(\theta_2))^2} + 1} - R_1 \cos(\theta_1) \sqrt{\frac{(R_1 \sin(\theta_1) - R_2 \sin(\theta_2))^2}{(-L + R_1 \cos(\theta_1) + R_2 \cos(\theta_2))^2} + 1} \right. \\ \left. - R_2 \cos(\theta_2) \sqrt{\frac{(R_1 \sin(\theta_1) - R_2 \sin(\theta_2))^2}{(-L + R_1 \cos(\theta_1) + R_2 \cos(\theta_2))^2} + 1} + R_1 + R_2 \right) - L \quad (\text{A1})$$

$$z_1 = R_1 \left( \cos(\theta_1) - \frac{1}{\sqrt{\frac{(R_1 \sin(\theta_1) - R_2 \sin(\theta_2))^2}{(-L + R_1 \cos(\theta_1) + R_2 \cos(\theta_2))^2} + 1}} \right) \quad (\text{A2})$$

$$x_1 = R_1 \left( \sin(\theta_1) + \frac{R_1 \sin(\theta_1) - R_2 \sin(\theta_2)}{(L - R_1 \cos(\theta_1) - R_2 \cos(\theta_2)) \sqrt{\frac{(R_1 \sin(\theta_1) - R_2 \sin(\theta_2))^2}{(-L + R_1 \cos(\theta_1) + R_2 \cos(\theta_2))^2} + 1}} \right) \quad (\text{A3})$$

$$z_2 = \frac{R_2}{\sqrt{\frac{(R_1 \sin(\theta_1) - R_2 \sin(\theta_2))^2}{(-L + R_1 \cos(\theta_1) + R_2 \cos(\theta_2))^2} + 1}} + L - R_2 \cos(\theta_2) \quad (\text{A4})$$

$$x_2 = R_1 \sin(\theta_1) + \frac{((R_1 \sin(\theta_1) - R_2 \sin(\theta_2)))}{-L + R_1 \cos(\theta_1) + R_2 \cos(\theta_2)} \times \left( \frac{R_2}{\sqrt{\frac{(R_1 \sin(\theta_1) - R_2 \sin(\theta_2))^2}{(-L + R_1 \cos(\theta_1) + R_2 \cos(\theta_2))^2} + 1}} + L - R_1 \cos(\theta_1) - R_2 \cos(\theta_2) \right) \quad (\text{A5})$$

### B. Full Form of Dithering Matrices

$$\begin{pmatrix} A_{ix} \\ A_{iy} \\ A_{ex} \\ A_{ey} \end{pmatrix}_p = \frac{2}{\alpha\gamma - \beta^2} \begin{pmatrix} -\beta - \gamma r & \alpha + \beta r & -\beta - \gamma r & \alpha + \beta r \\ -\beta - \gamma r & \alpha + \beta r & \beta + \gamma r & -\alpha - \beta r \\ \gamma - \beta r & \alpha r - \beta & \gamma - \beta r & \alpha r - \beta \\ \gamma - \beta r & \alpha r - \beta & \beta r - \gamma & \beta - \alpha r \end{pmatrix} \begin{pmatrix} C_{dh} \\ C_{ds} \\ C_{ch} \\ C_{cs} \end{pmatrix}_p \quad (\text{B1})$$

$$\begin{pmatrix} A_{ix} \\ A_{iy} \\ A_{ex} \\ A_{ey} \end{pmatrix}_y = \frac{2}{\alpha\gamma - \beta^2} \begin{pmatrix} \gamma r - \beta & \alpha - \beta r & \gamma r - \beta & \alpha - \beta r \\ \beta - \gamma r & \beta r - \alpha & \gamma r - \beta & \alpha - \beta r \\ \gamma + \beta r & r\alpha r - \beta & \gamma + \beta r & -\alpha r - \beta \\ -\beta r - \gamma & \beta + \alpha r & \gamma + \beta r & -\alpha r - \beta \end{pmatrix} \begin{pmatrix} C_{dh} \\ C_{ds} \\ C_{ch} \\ C_{cs} \end{pmatrix}_y \quad (\text{B2})$$

$$\begin{pmatrix} A_{ix} \\ A_{iy} \\ A_{ex} \\ A_{ey} \end{pmatrix}_p = 10^{-4} \begin{pmatrix} -0.346205 & 3.05472 & -0.346205 & 3.05472 \\ -0.346205 & 3.05472 & 0.346205 & -3.05472 \\ -0.418406 & 1.93982 & -0.418406 & 1.93982 \\ -0.418406 & 1.93982 & 0.418406 & -1.93982 \end{pmatrix} \begin{pmatrix} C_{dh} \\ C_{ds} \\ C_{ch} \\ C_{cs} \end{pmatrix}_p \quad (\text{B3})$$

$$\begin{pmatrix} A_{ix} \\ A_{iy} \\ A_{ex} \\ A_{ey} \end{pmatrix}_y = 10^{-4} \begin{pmatrix} 0.346205 & 3.05472 & 0.346205 & 3.05472 \\ -0.346205 & -3.05472 & 0.346205 & 3.05472 \\ -0.418406 & -1.93982 & -0.418406 & -1.93982 \\ 0.418406 & 1.93982 & -0.418406 & -1.93982 \end{pmatrix} \begin{pmatrix} C_{dh} \\ C_{ds} \\ C_{ch} \\ C_{cs} \end{pmatrix}_y \quad (\text{B4})$$

### C. Dithering Theory

This section is an example from Kawabe's discussion on how mechanical modulation is used to sense and actively suppress low frequency motion of test mass angles [10]. It aligns the beam axis with the cavity axis.

To simplify, both mirrors have the same radius of curvature. Let  $I$  be the intensity of reflected field. The following parameters are used:  $a(\nu)$  and  $a(\nu - \nu_{10})$  is cavity reflectance of the fundamental mode and the first higher mode respectively (which are both constant),  $a_x$  is the beam waist height and  $\alpha_x$  is the angle of misalignment of the incident beam and the cavity axis, and  $w_0$  is the width of the waist.

$$I = I_0 \left[ |a(\nu)|^2 + \gamma (|a(\nu - \nu_{10})|^2 - |a(\nu)|^2) \right] \quad (\text{C1a})$$

$$\gamma := \left( \frac{a_x}{w_0} \right)^2 + \left( \frac{k w_0 \alpha_x}{2} \right)^2 \quad (\text{C1b})$$



$$a_x = \frac{1}{2}(x_1 + x_2) \quad (\text{C1c})$$

$$\alpha_x = \frac{1}{2R - L}(x_2 - x_1) \quad (\text{C1d})$$

The modulations are:

$$x_1 = x_{10} + A_1 \sin \omega_1 t \quad (\text{C2a})$$

$$x_2 = x_{20} + A_2 \sin \omega_2 t \quad (\text{C2b})$$

Substituting these two modulations in the values for the beam waist displacement  $a_x$  and angle difference  $\alpha_x$  into equation (C1a), and taking a Taylor series to first order, the following result is found[10].

$$I \approx I_0 \left[ \left\{ |a(\nu)|^2 + \gamma(|a(\nu - \nu_{10})|^2 - |a(\nu)|^2) \right\} * \left\{ \gamma(x_{10}, x_{20}) + A_1 \sin \omega_1 t \frac{\partial \gamma}{\partial x_1} \Big|_{x_{10}} + A_2 \sin \omega_2 t \frac{\partial \gamma}{\partial x_2} \Big|_{x_{20}} \right\} \right] \quad (\text{C3})$$

Applying narrow bandpass filters around each modulation frequency and demodulating, the DC terms remaining are the two partial derivatives. When the partial derivatives are expanded, they take the following form.

$$\frac{\partial \gamma}{\partial x_1} \Big|_{x_{10}} = \frac{1}{2w_0^2} \left( x_{10} + x_{20} + \left( \frac{L}{kw_0^2} \right)^2 (x_{10} - x_{20}) \right) \quad (\text{C4a})$$

$$\frac{\partial \gamma}{\partial x_2} \Big|_{x_{20}} = \frac{1}{2w_0^2} \left( x_{10} + x_{20} - \left( \frac{L}{kw_0^2} \right)^2 (x_{10} - x_{20}) \right) \quad (\text{C4b})$$

The demodulation sensor returns the values of the partial derivatives of  $\gamma$  with respect to  $x_1$  and  $x_2$ , which is an error signal for the cavity. This is a linear system which can be solved for the center displacements. The misalignment signal it is sent to the actuators to align the cavity.

#### D. Flowchart of Calibration

The calibration steps are in figure 12.

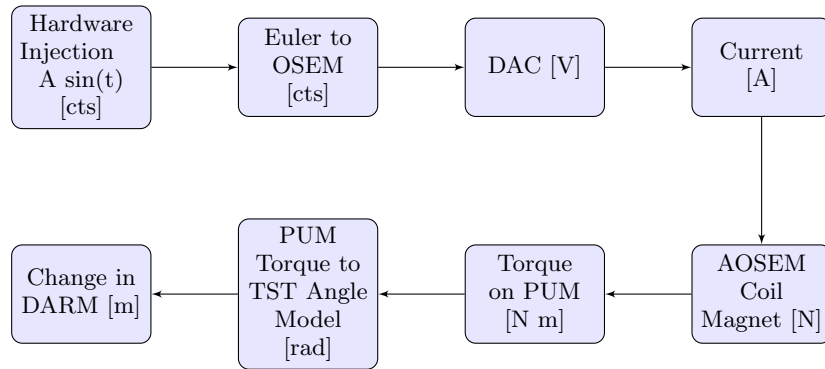


FIG. 12. This shows how we converted our modulation in counts into change in DARM.

### E. Interesting findings from CARM/Interpretation of formula for DARM

When the formula for CARM is calculated, the following pattern emerges: all angles are either common squared or differential squared. This relates to DARM because retrospectively it can be seen that it is the product of a common and differential angle. Thus, solely common-differential mode products couple into DARM.

$$\Delta CARM = \frac{2\theta_{ch}\theta_{cs}L(g_1r - g_2r + r^2 - 1)}{g_1g_2 - 1} + \frac{2\theta_{dh}\theta_{ds}L(g_1r - g_2r + r^2 - 1)}{g_1g_2 - 1} - \frac{\theta_{ch}^2L(r(g_1r - 2) + g_2)}{g_1g_2 - 1} - \frac{\theta_{cs}^2L(r(g_2r + 2) + g_1)}{g_1g_2 - 1} - \frac{\theta_{dh}^2L(r(g_1r - 2) + g_2)}{g_1g_2 - 1} - \frac{\theta_{ds}^2L(r(g_2r + 2) + g_1)}{g_1g_2 - 1} \quad (E1a)$$

$$\Delta CARM = -78095.7\theta_{ch}^2 + 23379.1\theta_{ch}\theta_{cs} + 1948.79\theta_{cs}^2 - 78095.7\theta_{dh}^2 + 23379.1\theta_{dh}\theta_{ds} + 1948.79\theta_{ds}^2 \quad (E1b)$$

### F. Wiener Filtering

#### 1. Wiener Filtering Theory Single Channel

Wiener filtering is a statistical technique to estimate a channel's true value. It is the optimal filter for the minimum mean squared error in linear, stationary systems [12]. The target channel's time series is  $x[m]$ . We have the sensor measurement,  $y[m]$ , of the target channel. The error is show in equation (F1), where the weights  $\vec{w}$  are to be found.

$$e[m] = x[m] - \hat{x}[m] = x[m] - \vec{w}^\top[m]\vec{y}[m] \quad (F1)$$

$$\vec{y}^\top[m] = \{y[m], y[m-1], \dots, y[m-P-1]\} \quad (F2)$$

$$\vec{w}^\top[m] = \{w[m], w[m-1], \dots, w[m-P-1]\} \quad (F3)$$

The optimum error is found by minimizing the squared error between target channel and estimator  $\hat{x}[m]$  in equation (F4).  $\vec{r}_{yx}$  is the cross correlation vector between witness and target signal, and  $\mathbf{R}_{yy}$  is the autocorrelation matrix between sensor signal  $\vec{y}$ .

$$\text{MSE} = \text{E} \{e[m]^2\} = \text{E} \{x[m]^2\} - 2\vec{w}^\top[m]\vec{r}_{yx} + \vec{w}^\top[m]\mathbf{R}_{yy}\vec{w}[m] \quad (F4)$$

The mean square error is optimized at the following filter value [13]:

$$\vec{w}[m] = \mathbf{R}_{yy}^{-1}\vec{r}_{yx} \quad (F5)$$

Figure 13 shows the process of wiener filtering graphically. Note the sensor does not sense a sum of the noise and target signal: in general  $y[m] = F(x[m], n[m], m)$ .

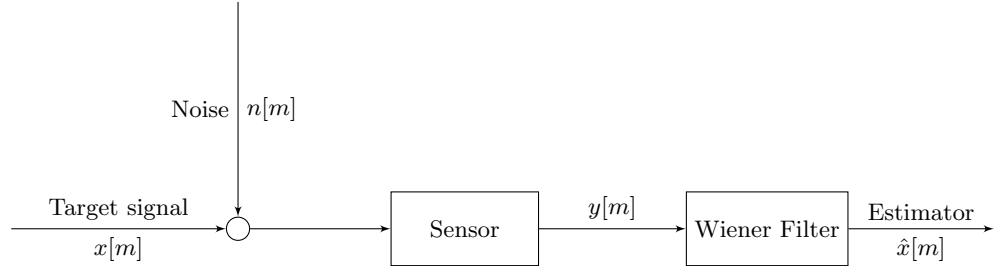


FIG. 13. A graphical representation of Wiener filtering.

Wiener filtering has important properties in the frequency domain. In the frequency domain, this condition for the Wiener filter becomes the following, where  $P_{xy}$  is the cross power spectral density [12]:

$$W(f) = \frac{P_{xy}}{P_{yy}} \quad (F6)$$

Additionally, the ideal suppression factor  $r(f)$  tells the amount each frequency is suppressed with a Wiener filter. It is dependent on witness coherence in equation (F7) [14]. For example at .9 coherence, the suppression factor is 2.3, meaning that the noise is reduced by a factor of 2.3.

$$r(f) = \frac{1}{\sqrt{1 - c(f)^2}} \quad (\text{F7})$$

## 2. Wiener Filtering Example for Additive Noise

Many times, the sensor's output can be approximated as additive uncorrelated noise [12]. Consider the following sensor profile:

$$y[m] = x[m] + n[m] \quad (\text{F8})$$

Taking the Fourier transform,

$$Y(f) = X(f) + N(f) \quad (\text{F9})$$

Taking the expectation value of the magnitude squared, and assuming that the target signal and noise are uncorrelated,

$$\text{E} \{|Y(f)|^2\} = P_{yy} = \text{E} \{|X(f)|^2\} + \text{E} \{|N(f)|^2\} = P_{xx} + P_{nn} \quad (\text{F10})$$

Since in uncorrelated additive noise,  $P_{xy} = P_{xx}$ , using equation (F6), the Wiener filter becomes:

$$W(f) = \frac{P_{xx}}{P_{xx} + P_{nn}} = \frac{SNR}{SNR + 1} \quad (\text{F11})$$

Equation (F11) gives a good explanation of how the Wiener filter is working. It is selecting frequencies when signal to noise ratio is high, while filtering frequencies when signal to noise ratio is low.

## 3. Multiple Sensor Wiener Filtering Theory

If there are multiple sensors with multiplicity M, the mean square error function to minimize is [15]:

$$\text{E} \left\{ e^2[m] \right\} = \text{E} \left\{ \left( x[m]^2 - \sum_{i=1}^{i=M} \vec{w}_i^T[m] \vec{y}_i[m] \right)^2 \right\} \quad (\text{F12})$$

The optimal filter weights for each sensor are shown in equation (F13) where  $\mathbf{C}_{ij}$  is the cross correlation matrix between sensor i and j,  $\mathbf{R}_{ii}$  is the autocorrelation matrix of sensor i,  $\vec{p}_{ix}$  is the cross correlation vector between the target channel and sensor i, and  $\vec{w}_i$  is the filter weights for sensor i [15].

$$\begin{bmatrix} \vec{w}_1 \\ \vec{w}_2 \\ \vdots \\ \vec{w}_N \end{bmatrix} = \begin{bmatrix} \mathbf{R}_{11} & \mathbf{C}_{12} & \cdots & \mathbf{C}_{1M} \\ \mathbf{C}_{21} & \mathbf{R}_{22} & \cdots & \mathbf{C}_{2M} \\ \vdots & & \ddots & \vdots \\ \mathbf{C}_{31} & \mathbf{C}_{32} & \cdots & \mathbf{R}_{MM} \end{bmatrix} \begin{bmatrix} \vec{r}_{1x} \\ \vec{r}_{2x} \\ \vdots \\ \vec{r}_{Mx} \end{bmatrix} \quad (\text{F13})$$

The estimation of the target channel is thus:

$$\hat{x}[m] = \sum_{i=1}^{i=M} \vec{w}_i^T[m] \cdot \vec{y}_i[m] \quad (\text{F14})$$

This approach is what we will use in the following sections to find the angular noise contribution to DARM.